International Journal of Hydrogen Energy 89 (2024) 161–176

Contents lists available at ScienceDirect

International Journal of Hydrogen Energy

journal homepage: www.elsevier.com/locate/he

Combination of G-Equation and Detailed Chemistry: An application to 3D-CFD hydrogen combustion simulations to predict NO_x emissions in reciprocating internal combustion engines

Stefano Sfriso [a,*], Fabio Berni [a], Stefano Fontanesi [a], Alessandro d'Adamo [a], Sebastiano Breda [a], Luigi Teodosio [b], Stefano Frigo [c], Marco Antonelli [c]

[a] Università Degli Studi di Modena e Reggio Emilia, Italy
[b] Università Federico II di Napoli, Italy
[c] Università di Pisa, Italy

ARTICLE INFO

Handling Editor: Dr C O Colpan

ABSTRACT

In the recent years, the growing pressure by the European Union to phase out the internal combustion engines has raised the quest for alternative solutions for low-environmental-impact mobility. Nevertheless, concerns on the life-cycle emissions of battery electric vehicles and perplexities on the socio-economic sustainability of the ecological transition suggest that maintaining the interest in internal combustion engines can be strategic, provided that carbon-neutral fuels are adopted. On the basis of the technological neutrality principle, relying on already existing and well-established technologies requires less effort and cost to convert the whole road transport. Moreover, the adoption of bio- or e-fuels obtained from renewable sources widely spread across the globe is not of secondary importance. In fact, cost reduction and worldwide diffusion of the resources are both main promoters of socio-economic sustainability.

In this scenario, green hydrogen represents one of the main solutions for the survival of reciprocating engines. Since the production is solely based on renewable energy sources, it is not simply characterized by zero CO_2 emissions at the tailpipe, but it can be considered overall carbon neutral. A technical drawback in the use of hydrogen is represented by emissions of nitrogen oxides (NO_x), due to the ever-present high temperature combustion process. For this reason, an ad-hoc design is mandatory to minimize NO_x production, and CFD can be a valid tool to reduce cost and time to market for the development of hydrogen engines.

In this regard, the current work proposes a 3D-CFD numerical methodology, based on the combination of G-Equation and Detailed Chemistry models, for NO_x prediction in in-cylinder simulations of reciprocating internal combustion engines fueled with hydrogen. Although the combination of level-set method and chemical kinetics is not a novelty in literature, it is the first time that it is applied to evaluate NO_x emissions in H_2 engines. The proposed approach is validated against experimental data on a direct injection, spark ignition, hydrogen engine. The methodology is able to properly predict NO_x emissions at different mixture qualities, revving speeds and spark times. The total number of investigated cases is 17, which is a large set of simulations compared to the existing literature. Considering the best chemical mechanism (i.e. the one providing the best results among the tested ones), the error in the NO_x prediction is always lower than 25% for all the simulations.

Once the methodology is validated, the effect of spark and injection timings on NO_x is discussed. Such a deepening is useful to emphasize the potential of the CFD to investigate phenomena leading to emission formation and, thus, to optimize engine parameters for NO_x reduction.

1. Introduction

Hydrogen reciprocating Internal Combustion Engines (ICEs) are currently re-gaining interest in the scientific community as well as in the industrial field. They are recognized as a possible way to guarantee a cleaner power generation during the ecological transition towards

* Corresponding author.
E-mail address: stefano.sfriso@unimore.it (S. Sfriso).

https://doi.org/10.1016/j.ijhydene.2024.09.252
Received 23 May 2024; Received in revised form 12 September 2024; Accepted 18 September 2024
Available online 26 September 2024

sustainable technologies. The use of green hydrogen (produced by renewable sources) in reciprocating ICEs can be of interest for specific applications. For example, when the mileage is a limit for a battery-powered electric vehicle, H_2 ICE can be a valuable stand-alone alternative or adopted as range extender. It is also valid for energy production in small power plants, where the high efficiency even under load variations and the relatively simple architecture make the internal combustion engine competitive with respect to turbomachinery [1,2]. Fairly, the conversion from electric power to hydrogen and then back to electric power by combustion in reciprocating engines implies a strong energy loss. Nonetheless, the need of energy storage and the possibility to provide it back during request peaks are strategic for a proper usage of renewable energy sources. From a social and economic standpoint, the widespread availability of primary sources around the globe is a significant advantage for its adoption. The decentralization of primary sources and power generation promotes, in fact, greater sustainability. H_2 ICEs are, in this picture, among the most balanced solutions considering ease of transition to green economy and pollutant abatement.

The challenge in the adoption of hydrogen as a fuel in ICEs is to adequately exploit the positive aspects while minimizing drawbacks. Considering the H_2 main properties available in literature [3–6], it is possible to take advantage of the very high Laminar Flame Speed (LFS) to increase both combustion and indicated efficiencies. Alternatively, the wide flammability range can be exploited to operate hydrogen ICEs in a diesel-like manner [7], thus further increasing the efficiency [8]. Moreover, both the LFS values and the flammability range mentioned above enable extremely lean combustions that minimize NO_x emissions. Another peculiar characteristic of H_2 is the low Lewis number that leads to the onset of thermo-diffusive instabilities. Such phenomena typically occur at equivalence ratio values lower than roughly 0.75 [6] and they cause, in turn, a strong increase of the laminar burning velocity with the positive effects mentioned above. Fairly, under turbulent conditions, it is still unclear to which extent the additional flame wrinkling due to instabilities can increase the flame speed compared to the turbulence effects [9–11]. Still on the H_2 advantages, the low quenching distance can increase the combustion efficiency as it allows the flame to burn the mixture in narrow crevices and very close to the walls. Finally, the very low minimum ignition energy ensures mixture ignition even at very lean conditions.

However, as previously anticipated, it is necessary to minimize the drawbacks, such as the decrease of the adiabatic efficiency resulting from the close proximity of the flame to the chamber walls. Moreover, the low ignition energy promotes pre-ignitions [12] that are a well-known problem of H_2 ICEs [13]. One of the main drawbacks in the use of H_2 is represented by NO_x emissions. Despite unburnt hydrocarbons, CO, CO_2 and soot are nominally eliminated among the combustion products, nitrogen oxides can potentially be present with high concentrations if slightly lean mixtures (i.e. φ values close to 0.8) are adopted. The reason is related to the high adiabatic flame temperature of H_2. The main strategy to reduce NO_x emissions relies on the use of very/ultra lean mixtures in combination with injection timings able to optimize the stratification of the charge. Tailpipe NO_x production represents also the main drawback of ammonia. The latter could be a valid alternative to H_2 for ICEs fueling, with the same advantages in terms of carbon neutrality and sustainability. In addition, NH_3 is characterized by easier storage. However, the presence of nitrogen in the molecule [14] implies a massive formation of NO_x during combustion. In fact, while H_2 forms nitrogen oxides because of the high temperatures of the burnt gases (thermal NO_x), ammonia forms the same pollutants as a consequence of the composition (fuel NO_x). Therefore, it is not possible to work on engine parameters (such as equivalence ratio) to drastically abate the nitrogen oxides. For completeness, it is useful to point out that NO_x are not the only drawback of NH_3. In fact, it has a very low laminar flame speed, which makes the engine design challenging [15], and it requires high ignition energy. In order to overcome the ignition difficulties, hydrogen may be added to ammonia. However, onboard generation of hydrogen from ammonia is not trivial [16]. Finally, ammonia is toxic.

3D-CFD can be proficiently adopted to investigate, for example, the capabilities of lean mixtures and ad-hoc injection strategies to suppress NO_x formation in H_2 ICEs. However, NO_x estimation in hydrogen combustion by in-cylinder simulations is far from being trivial. Besides an ad-hoc modeling for the emission formation, it is necessary to have a robust methodology able to properly simulate gas injection, mixture formation and combustion. In-cylinder simulations of H_2 ICEs with focus on combustion and NO_x emissions are not a novelty in the scientific literature, where multiple combinations of combustion and NO_x models are adopted. For example, Rakopoulos [17] and Kosmadakis [18] exploit an in-house developed combustion model and Zel'dovich mechanism to predict performance and NO_x formation. They also validate the numerical results against experimental outcomes. Hairong et al. [19] rely on Detailed Chemistry (DC) for both combustion and NO_x prediction. Chun et al. [20] still adopt DC for combustion but Zel'dovich mechanism for NO_x estimation. Maio et al. [21] correlate CFD outcomes and experimental data in terms of combustion and emissions using ECFM and Zel'dovich mechanism, but at the expense of a case-by-case calibration of the setup. Berni et al. [22] investigate NH_3–H_2 mixtures and combine G-Equation (for flame propagation) and DC (in the burnt region) for a proper estimation of both combustion and nitrogen oxides. Despite the combination of G-Equation and DC is already validated in literature (for both combustion and NO_x emissions) in case of gasoline and propane [23,24], unfortunately no experimental data is presented in Ref. [22] to support the numerical outcomes in presence of H_2.

In view of the literature review proposed above, it is possible to infer that, in case of H_2 combustion, a thorough validation of G-Equation combined with DC is not available. Therefore, the present paper aims at filling this gap, to demonstrate the capabilities of such numerical methodology. Compared to the other approaches found in literature and outlined above, it is authors' opinion that the combination of G-Equation and DC (in the burnt region) can be an optimal solution to properly estimate both H_2 turbulent premixed (or partially premixed) flame propagation and NO_x emissions, at least in the flamelet regime. In fact, unlike pure DC approaches, G-Equation is purposely developed to predict flame wrinkling at this condition. Moreover, compared to a simplified approach based on Zel'dovich model, DC is more accurate to predict NO_x in the burnt region. In the present paper, the approach is validated on different operating points, by comparing numerical and experimental data in terms of in-cylinder pressure, combustion indicators and NO_x emissions. Interestingly, considering the variations of equivalence ratio, revving speed and spark-time, 17 validation cases are proposed in the present manuscript. This set of cases is among the most extended ones available in literature (not to say the most extended one). For example, considering the papers cited above, Rakopoulos et al. [17] validate on 6 cases. The same number of points is proposed by Kosmadakis et al. [18]and Hairong et al. [19]. Chun et al. [20] propose only one case. Therefore, although the proposed methodology is not characterized by a higher precision in terms of NO_x estimations compared to the existing literature, in the present paper it undergoes an extensive validation which has no equal in other works. Moreover, on the same cases, the validation deals with combustion and nitrogen oxides emissions, i.e. the attention is simultaneously focused on both the aspects. Finally, the agreement between CFD and test bench measurements across the different conditions is sought after without case-to-case calibration of the models, which is another noteworthy aspect compared to the literature.

The current paper represents a development of a work previously published by the authors [25]. Compared to Ref. [25], where the emissions were not considered, in this paper the 3D-CFD numerical methodology is improved by introducing DC to predict NO_x production. Moreover, although the investigated engine is basically the same, in this case the injection pressure is doubled and injector nozzles are different.

After the introduction, experiments are described. Subsequently, the

CFD model is proposed and then validated against experiments. Before the conclusions, a deepening on the obtained results in terms of NO_x emissions is proposed. In particular, the impact of spark and injection timings is discussed to highlight the potential of the CFD.

2. Experimental apparatus and data

The experimental activity starts with the adaptation of the original engine to H_2 injection and combustion [26]. The production Diesel engine, namely Lombardini 15LD500, was developed nearly 20 years ago for several light duty applications. Table 1 provides details of the engine specifications before and after the conversion.

The conversion to H_2 involves the adoption of two low-pressure injectors (operated at 12 bar), a spark-plug for mixture ignition and a reduction of the geometric compression ratio (CR) from 19:1 to 10:1. The CR reduction is achieved by a broader piston bowl, which is shown in Fig. 1, and inserting a spacer between crankcase and cylinder. In order to mount the two H_2 injectors, an external portion of the engine head is flattened. Fig. 2 reports the cylinder head with the additional components used for the conversion.

Table 2 resumes the experimental operating conditions replicated by the numerical simulations. They include different revving speeds, equivalence ratios (hence loads) and spark times.

A schematic representation of the test rig is depicted in Fig. 3. The complete system is positioned on the test bench and the engine output shaft is connected to a "Borghi e Severi" eddy current dynamometer, controlled by an API microprocessor unit. In order to obtain the indicated cycle, pressure is measured by the Kistler 6052C piezoelectric high temperature sensor, with a nominal sensitivity of nearly −20 pC/bar and a pressure range of 250 bar, featuring a maximum linearity error of ±0.4% of the full-scale output. The crankshaft position measurement relies on the 365X AVL angle encoder with ±0.1°CA precision. The signals of in-cylinder pressure sensor and encoder are processed by the AVL IndiCom 1.2 acquisition code, in order to obtain the indicated cycle. The electronic control of injection and ignition is entrusted to the engine control unit (ECU), namely the Motec M400. In the exhaust line, the Bosch LSU 4.2 wide-band lambda sensor is installed to evaluate the equivalence ratio. Due to the strong sensitivity of the lambda sensors to H_2 operation, three probes are alternated during the tests to keep the measurement accuracy within ±5%. To reduce the uncertainty of the data, φ values are verified by mass flow rate data of both intake air and H_2. Fuel and intake air mass flow rates are obtained by the Bronkhorst High-Tech EL-FLOW mass flow meter. To calibrate the lambda sensors, a suitable range of mixture qualities is firstly individuated based on the engine conditions. Then, a mixture with the highest equivalence ratio of the defined range is imposed in the engine with the help of the mass flow meters. Given the voltage signal of the lambda sensor, the corresponding output value is scaled to match the imposed one. This procedure is repeated at steps of 0.1 till the lower equivalence ratio and the measure is checked for different days to account for the specific ambient conditions. The calibration is considered satisfactory if the measure remains within a ±5% error without adjustments for all the days. The test bench also monitors the temperatures of intake air, exhaust gas and injected H_2 by thermocouples. The Beckman 951 chemiluminescence analyzer is used to measure NO_x emissions, which is characterized by an accuracy of ±0.5% of full scale. Gases are sampled by a probe installed in the exhaust line. Further details on the experimental apparatus can be found in Ref. [27].

Table 1
Stock and modified engine specifications.

	Diesel	Hydrogen
N° of Cylinders	1	1
Valves per cylinder	2	2
Alimentation	Naturally aspirated	Naturally aspirated
Bore	87 mm	87 mm
Stroke	85 mm	85 mm
Displacement	505 cm^3	505 cm^3
Compression ratio	19:1	10:1
Max Power	9 kW @ 3600 rpm	9.1 kW @ 3000 rpm
Max Torque	31 Nm @ 2000 rpm	32.7 Nm @ 2500 rpm
Combustion initiation	CI	SI

Fig. 1. Piston with modified bowl [26].

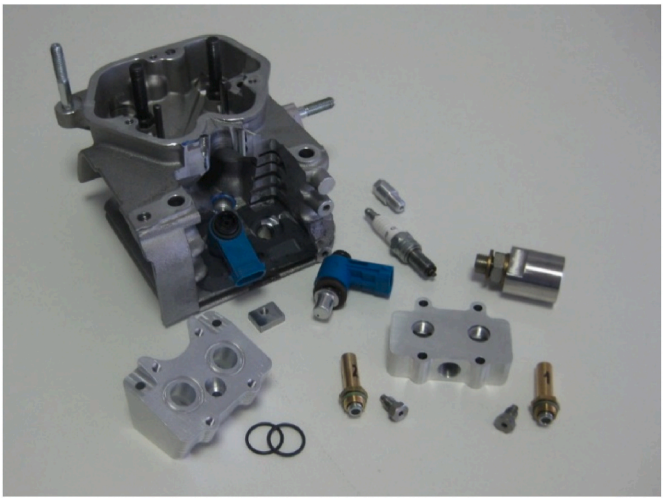

Fig. 2. Modified head and additional components such as hydrogen injectors and spark plug [27].

3. CFD model

The numerical methodology adopted in the present work is derived from a simpler version previously validated by the authors on the same engine operated at multiple speeds and equivalence ratios [25]. In Ref. [25], simplicity and reliability are the pillars governing the methodology development. In this regard, the adoption of G-Equation for

Table 2
Test bench operating conditions; a negative ST means that ignition occurs before the TDCF.

Test N°	φ	SOI [° CA bTDCF]	p H_2 [bar]	Speed [rpm]	Spark Time [° CA]
1	0.8	225	12	3000	0
2					3
3					6
4					9
5					12
6	0.6	190	12	3000	−15
7					−12
8					−9
9					−6
10					−3
11					0
12					3
13	0.8	175	12	2000	0
14					3
15					6
16					9
17					12

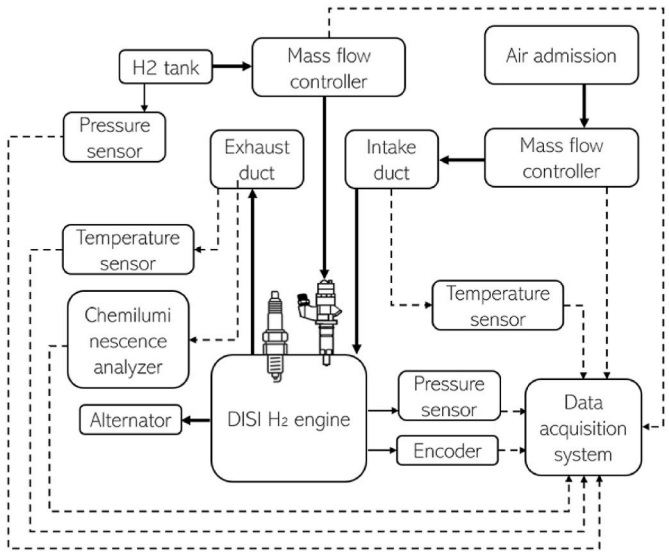

Fig. 3. Test bench scheme.

combustion modeling is due to the predictive capabilities without (or with minimal) case-to-case tuning of the model constants. The same is not valid for other well-consolidated combustion models, such as ECFM-3Z which requires, based on the authors' experience with it, significant calibration when the operating conditions considerably change. Also pure DC is not considered in Ref. [25], but in this case the choice is governed by theoretical considerations. In fact, the flamelet combustion regime that usually characterizes the ICEs along with a computational grid not able to fully resolve the turbulent phenomena prohibit the adoption of pure DC and require the modeling of the turbulence-flame interaction. Compared to Ref. [25], in the present work the authors increase the methodology complexity by introducing DC model in the burnt gases, to accurately compute their composition and predict NO_x emissions. The most challenging aspect of the new methodology deals with chemical mechanism. It is necessary to select an effective skeletal mechanism able to ensure accuracy and simultaneously limit the computational effort. A detailed description of the CFD model is presented hereafter.

The solver adopted for the in-cylinder simulations is STAR-CD, licensed by SIEMENS DISW. The reason for this choice is the long-time experience of the authors with this software which leaded, in the last two decades, to the in-house development of multiple models (such as the heat transfer and ignition ones adopted in the present work). A URANS approach to turbulence is adopted, closing the Navier-Stokes equations with the k-ε RNG model [28,29], which is used as extensively adopted in the literature and in previous publications by the authors [30–35]. A high-Reynolds wall treatment is preferred to limit the computational cost. The Improved GruMo-UniMORE heat transfer model [36–38] developed by the authors and implemented in STAR-CD is used. This model accounts for the actual Prandtl number of the mixture and effectively predicts wall heat fluxes regardless of the near-wall grid resolution. The time step is set to 0.05° CA (corresponding to 2.77×10^{-6} s at 3000 rpm and 4.16×10^{-6} s at 2000 rpm) during valve opening and closing, injection and combustion, while 0.1° CA (corresponding to 5.54×10^{-6} s at 3000 rpm and 8.32×10^{-6} s at 2000 rpm) is adopted in the remaining portions of the cycle. Experimental pressure and temperature values are assigned to intake and exhaust boundaries. The mass flow rate applied at both the H_2 inlet boundaries (in correspondence of the injectors) follows an experimentally derived trapezoidal law. The adopted wall temperatures are reported in Table 3 and are based on the authors' experience on both spark ignition and compression ignition engines [39–41]. The simulations start at 90°CA aTDC and end at 810°CA aTDC. Then, for each operating point, multiple consecutive cycles are simulated to eliminate the effect of the initial conditions and obtain a converged solution, i.e. no significant cycle-to-cycle difference can be noticed.

3.1. Mesh

The mesh size ranges between 1 and 2 mm in the core. Ad-hoc refinements are carried out around the spark-plug (the cell size is halved) and in correspondence of the injectors (the cell size is reduced to 1/32 of the core mesh, leading to a minimum size of nearly 30 μm). With this setup, the maximum number of cells at BDC is 927 k. The adopted numerical grid is reported in Fig. 4. A detail of the injector internal geometry included in the domain as well as the mesh utilized for the discretization are visible in Fig. 5. At the walls, a single 0.3 mm thick prismatic layer is adopted.

3.2. Ignition

Ignition is simulated by an in-house model which is developed and extensively validated in LES approach [42,43]. A simplified RANS version of the model is adopted in the present work, in which the impact of the electric circuit delay on the flame kernel deposition is neglected. In fact, as reported in literature [44–46], the time between nominal spark time and effective breakdown is in the order of 10 μs (to be considered as an order of magnitude), which is negligible at the investigated revving speed.

The growth of flame kernel after the spark event is governed by a 1D model represented by Eq. (1), which is similar to the Herweg and Maly one [47].

$$\frac{dr_k}{dt} = \frac{\rho_u}{\rho_k}(S_L + S_{Plasma}) + \frac{V_k}{A_k}\left[\frac{1}{T_k}\frac{dT_k}{dt}\right] \quad (1)$$

r_k is the kernel radius and ρ_u is density of the unburned gases. ρ_k and T_k

Table 3
Wall temperatures.

Combustion dome	523 K
Piston crown	523 K
Cylinder wall	453 K
Intake valve stem and port	320 K
Intake valve face	420 K
Exhaust valve stem	720 K
Exhaust valve face	720 K
Exhaust port	473 K
Spark plug	600 K

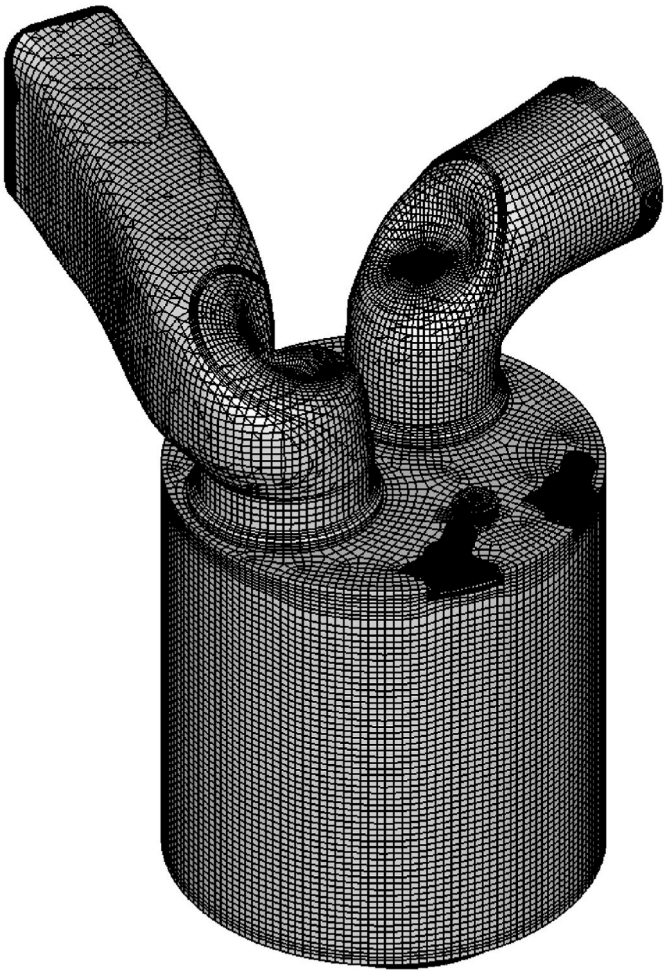

Fig. 4. Computational mesh at BDC.

are mean density and temperature of the kernel, respectively. V_k and A_k are volume and surface of the kernel. S_L and S_{Plasma} are laminar flame speed and expansion velocity of the plasma channel. Compared to the Herweg and Maly model, no transition function from laminar to turbulent flame speed is introduced and only the laminar one is used. When the flame kernel size is equal to 2 mm, the ignition model switches off and G-Equation activates. In fact, after that size, turbulence contribution becomes significant [47] and the above 1D model loses accuracy.

The value of S_{Plasma} is determined by solving the one-dimensional unsteady heat conduction equation (assuming a spherical kernel initiation) proposed in Eq. (2), still similarly to the Herweg and Maly model.

$$\rho c_p \frac{\partial T}{\partial t} = \frac{\partial}{\partial x}\left(k \frac{\partial T}{\partial x}\right) \tag{2}$$

ρ and c_p are density and specific heat, respectively. T and t are temperature and time, x is the radial coordinate while k is the thermal conductivity. As for the plasma properties, ρc_p is here fixed to 8000 J/(m^3K) and the thermal conductivity to 0.2 W/(mK) [48–53]. The boundary condition of Eq. (2), that is the temperature at $x = 0$, is set equal to $60 \bullet 10^3$ K [47]. Basically, Eq. (2) aims at investigating the velocity of temperature diffusion along a specific direction starting from a high-temperature source (corresponding to the plasma channel) and this velocity is assumed as S_{Plasma}.

The initial value of r_k (i.e. the initial condition for Eq. (1)) is estimated similarly to Ref. [54]. A volume of burnt mass is computed as the volume of a cylinder with height equal to the spark gap (d_{gap}, equal to 0.5 mm for this case) and radius equal to the flame thickness δ_L. The initial radius of the spherical flame kernel is then computed following Eq. (4), i.e. it is the radius of the sphere having the volume computed in Eq. (3).

$$V_{k,init} = d_{gap} \pi \delta_L{}^2 \tag{3}$$

$$r_{k,init} = \left(\frac{3}{4\pi} V_{k,init}\right)^{1/3} \tag{4}$$

δ_L values are computed for the investigated operating conditions using 1D steady-state freely propagating flame simulations conducted in DARS v2020.1 licensed by SIEMENS DISW. The governing equations for the freely propagating flame model can be found in the DARS manual [55]. The kinetics mechanism proposed by Shrestha [56] is employed for the simulations. Values of pressure, temperature and equivalence ratio for the 1D simulations are derived from both 3D simulations and experimental data. Pressure and temperature are calculated as mass-weighted averages within the combustion chamber at spark time. Equivalence ratio values correspond to the nominal values. EGR is not considered due to the negligible concentration. The investigated conditions in the 1D simulations are resumed in Table 4.

The resulting flame kernel sizes, computed from the laminar flame thickness δ_L according to Eq.s (3) and (4), are reported in Fig. 6. Since, for all the conditions, pressure, temperature and equivalence ratio are similar, the initial kernel radius is roughly characterized by the same size, equal to $2 \bullet 10^{-5}$ m. For this reason, such value is adopted as the initial condition for the kernel development equation in the ignition model. A sensitivity to this value, not reported for brevity, points out that no significant variation of the results is noticed for small variations of the initial value of r_k. In other words, it is sufficient to consider a proper order of magnitude for it, as the kernel growth is then fast enough to compensate possible variations.

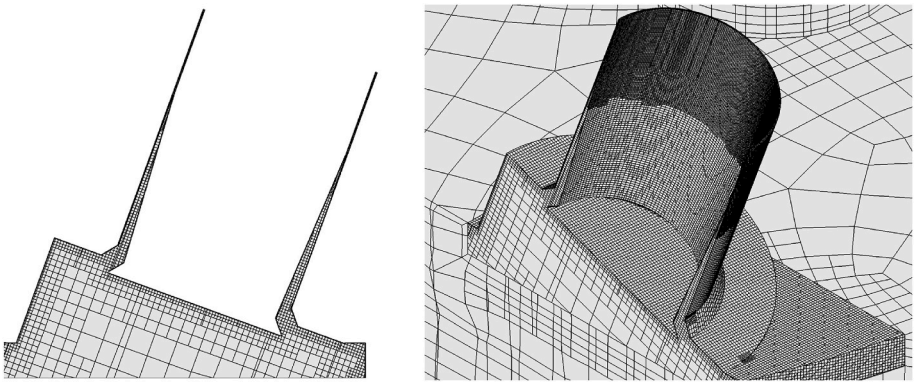

Fig. 5. Detail of the mesh in correspondence of the injector.

Table 4
Equivalence ratio, pressure and temperature, at ST, for the different operating conditions.

Engine speed [rpm]	φ	P [bar]	T [K]	ST [° CA]
2000	0.8	26.4	849	0
		26.0	843	3
		25.0	833	6
		23.7	819	9
		22.0	801	12
3000	0.6	19.3	831	−15
		20.9	846	−12
		22.3	858	−9
		23.4	866	−6
		24.1	869	−3
		24.2	868	0
		23.9	862	3
3000	0.8	25.2	853	0
		24.8	848	3
		23.9	838	6
		22.7	824	9
		21.1	806	12

3.3. Combustion

As stated earlier, turbulent premixed (or partially premixed) combustion is simulated using the flamelet G-Equation model, based on a level-set method which distinguishes burned and unburned regions by an iso-surface of the scalar G, denoted as the G = 0 surface. This surface solely indicates the flame front position. To simulate the flame structure in turbulent flows, it is necessary to consider the variance of G, which provides information to calculate the turbulent flame brush thickness. Eq. (5) represents the transport equation of G (while the transport equation for its variance is not reported for brevity).

$$\frac{\partial}{\partial t}\rho G + \frac{\partial}{\partial x_i}\rho u_i G = \rho S_T |\nabla G| \tag{5}$$

A regress variable (c), ranging from 1 (in the unburnt mixture) to 0 (in the fully burnt mixture), is calculated via the turbulent flame brush thickness and it is exploited to account for the presence of a flame brush. Further details can be found in Refs. [25,57]. When the G = 0 iso-surface starts to propagate, c decreases. Once the regress variable falls below 0.99, the Detailed Chemistry model is activated. This model is specifically designed to integrate detailed chemical kinetics into engine simulations. In other words, the chemical kinetics is online solved instead of being tabulated (i.e. calculated offline). DC relies on both transport equations for all the species, such as the one reported in Eq. (6), and a comprehensive reaction mechanism.

$$\frac{\partial}{\partial t}(\rho Y_i) + \frac{\partial}{\partial x_i}(\rho u_j Y_i - F_{i,j}) = S_i \tag{6}$$

Y_i is the mass fraction of the i-th species, x_i the i-th coordinate, u_j the j-th velocity component, $F_{i,j}$ the diffusion flux component and S_i represents the production/consumption rate of the i-th species. To derive an expression for S_i, it is necessary to introduce a detailed multi-step chemical reaction mechanism as in Eq. (7), including N chemical species and N_R reactions.

$$\sum_{k=1}^{N}(\nu'_{Rk}R_k) = \sum_{k=1}^{N}(\nu''_{Rk}R_k), R = 1, 2, \ldots, N_R \tag{7}$$

ν'_{Rk} and ν''_{Rk} represent the stoichiometric coefficients for reactants and products, respectively. Their subscript (Rk) indicates k-th species and reaction R. R_k is the chemical symbol of the k-th species. The production/consumption rate of the i-th species is described in Eq. (8).

$$S_i = M_i \sum_{R=1}^{N_R}\left[(\nu''_{Ri} - \nu'_{Ri})\left(k_{fR}\prod_{k=1}^{N}[R_k]^{\nu'_{Rk}} - k_{rR}\prod_{k=1}^{N}[R_k]^{\nu''_{Rk}}\right)\right] \tag{8}$$

M_i represents the molecular weight of the i-th species, while ν'_{Ri} and ν''_{Ri} have the same meaning as ν'_{Rk} and ν''_{Rk} , respectively. $[R_k]$ denotes the mole concentration, while k_{fR} and k_{rR} stand for forward and backward rate constants of reaction R. The DC approach is utilized to estimate emission formation. For instance, in case of NO_x, transport equations for NO and NO_2 enable the monitor of production and consumption of these scalars.

Regarding the chemical schemes utilized in the 3D in-cylinder simulations with DC, the widely validated mechanisms proposed by Shrestha [58] and Klippenstein [59] are tested, and their results are compared. This is purposely done to investigate the sensitivity of the results to the chemical scheme.

For the propagation of the G = 0 iso-surface, the turbulent flame speed S_T is required in Eq. (5) and it is computed by the Damköhler-derived correlation [60] reported in Eq. (9).

$$S_T = S_L\left(1 + A \bullet \left(\frac{u'}{S_L}\right)^{\frac{5}{6}}\right) \tag{9}$$

S_L is the unstretched laminar flame speed, u′ is the root-mean-square of the turbulent velocity fluctuations. A is an empirical coefficient equal to 2.2. S_L is calculated using the correlation proposed by Verhelst [61], which is valid for p, T, φ and EGR ranges equal to 5 bar ≤ p ≤ 45 bar,

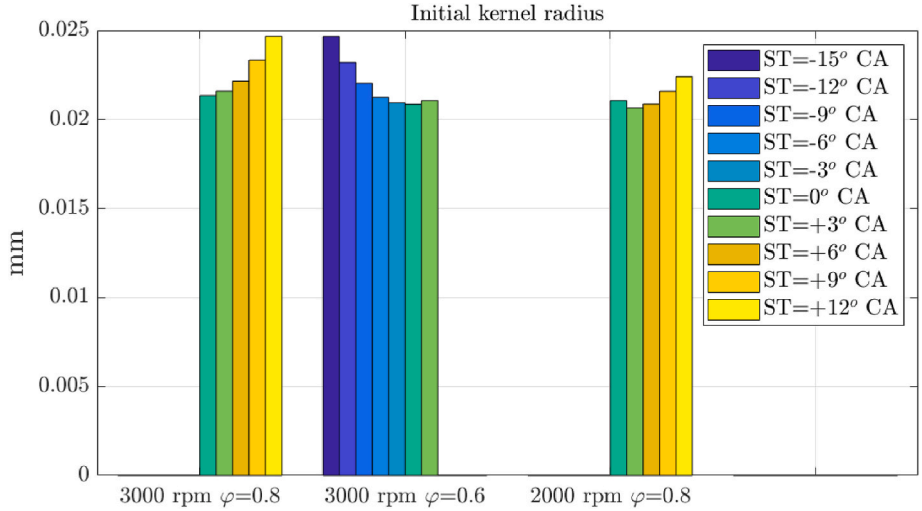

Fig. 6. Initial radius values for all the operating conditions; each bar corresponds to a different ST.

500 K ≤ T ≤ 900 K, 0.33 ≤ φ ≤ 5, 0% ≤ EGR ≤50%. Therefore, it is valid throughout the conditions of the experiments here utilized.

Different studies in literature emphasize the significant impact of the thermo-diffusive instabilities on the flame speed in hydrogen combustion. For instance, after a rigorous theoretical analysis, Atlantzis et al. [62] and Matalon et al. [6] highlight the influence of such instabilities on the flame speed at laminar conditions but, simultaneously, they express uncertainty regarding the effect at turbulent conditions. Other publications show the influence of the instabilities also in turbulent flows. For example, Berger et al. [63] observe the effect of the interaction between thermo-diffusive instability and turbulence on the flame speed in a DNS combustion simulation carried out at ambient pressure and temperature and lean mixture. However, the conditions investigated by Berger et al. differ significantly from those commonly found in engines. Consequently, the actual influence of the instabilities at engine-like conditions (i.e. at high pressure, temperature and turbulence) currently remains a topic of debate. In this regard, preliminary attempts to include the instabilities in engine simulations are available

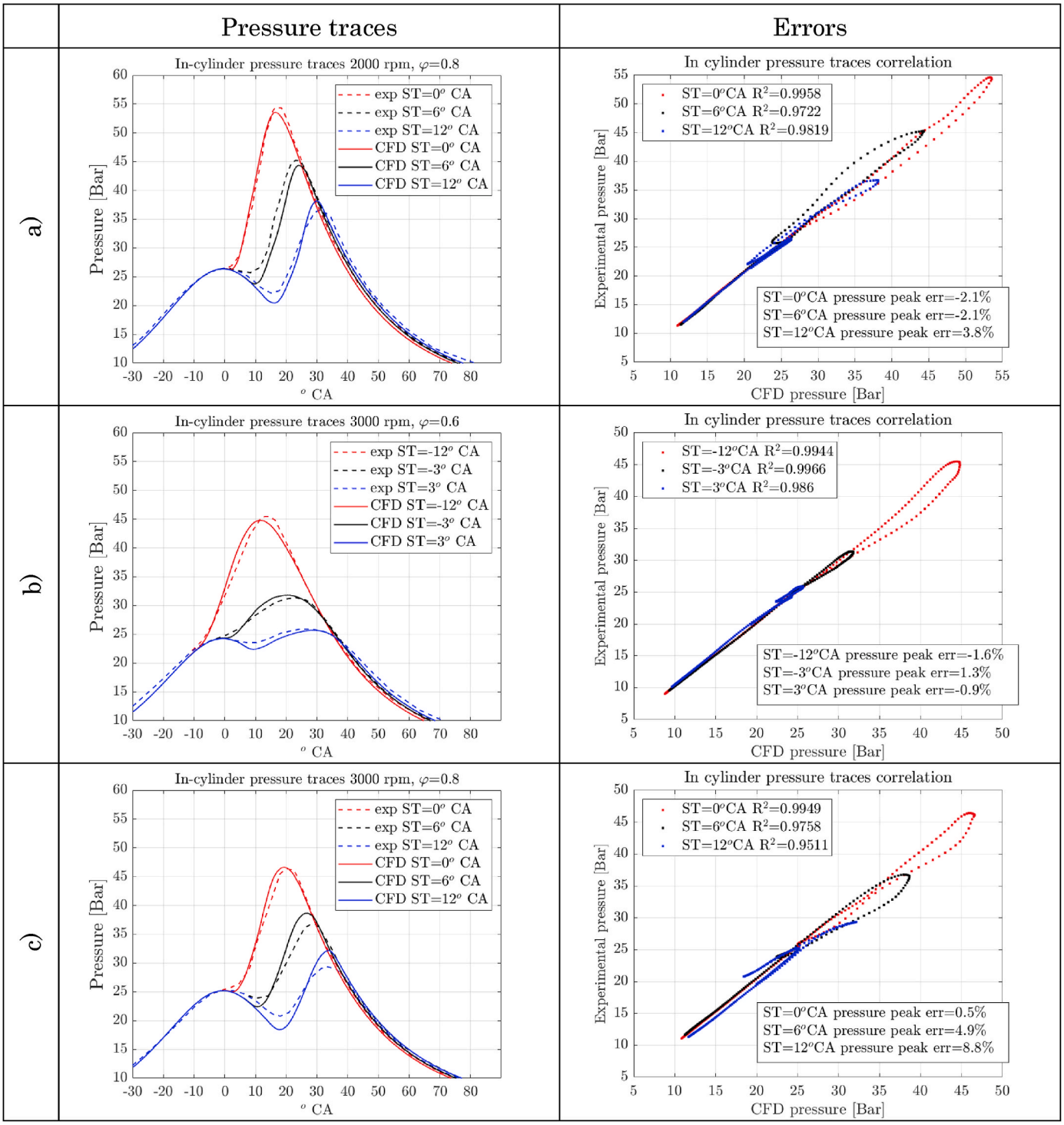

Fig. 7. Comparison between measured and computed in-cylinder pressure traces for a) 2000 rpm - φ = 0.8 case, b) 3000 rpm - φ = 0.6 case and c) 3000 rpm - φ = 0.8 case.

in literature. Hernandez et al. [64] include the instability effect in 3D-CFD combustion simulations of a hydrogen engine, with modest impact on the results. Instead, De Bellis et al. [65] strongly enhance the result accuracy by including the instability effect in 1D simulations of an H_2 engine. Conversely, in a previous publication by the authors of the present paper [25], satisfying results over a wide set of conditions ($0.4<\varphi<0.8$ and $1500<rpm<3000$) are obtained investigating by 3D-CFD a hydrogen engine without including thermo-diffusive instabilities. Therefore, given the existing literature just discussed (from which it is not possible to univocally sentence about the thermo-diffusive instability effect at engine-like conditions) and coherently with the previous publication by the authors, in the present work the thermo-diffusive instabilities are not accounted for either in the laminar flame speed or in the turbulent one. This choice is also coherent with recent experimental observations proposed in Ref. [66] on a hydrogen engine operated at ultra-lean conditions. In Ref. [66], it is shown that it is possible to match the experimentally measured turbulent flame speed, starting from the unstretched S_L and adopting a Damköhler-derived correlation for S_T (corresponding to Eq. (9) unless the constants), completely neglecting the instability representation. Finally, as a further support to the choice, in Ref. [67] the authors of the present paper show that it is possible to obtain good results, at engine-like conditions and neglecting the thermo-diffusive instability effect, even in case of ultra-lean hydrogen mixtures (i.e. at $\varphi = 0.3$, where the effect should be stronger), still adopting unstretched S_L and Damköhler-derived correlation for S_T.

4. Results

4.1. Numerical methodology validation

The first part of the result section is dedicated to the validation of the proposed numerical methodology. In particular, since the NO_x formation is closely related to the combustion process, it is necessary to assess the capabilities of the CFD model to properly predict such phenomenon at first. For that purpose, numerical and experimental pressure traces are compared during the high temperature portion of the engine cycle and they are reported in Fig. 7. For each of the tested operating conditions, the results of three different spark times are shown.

A satisfactory agreement between CFD outcomes and experimental evidences is obtained, which is noteworthy considering that no case-by-case calibration of the model constants is carried out. The 3D model is able to properly reproduce the trend of the in-cylinder pressure as a function of the spark time. In order to provide a more quantitative comparison between simulated and experimental pressures, in the second column of Fig. 7 an error analysis is proposed. The coefficient of

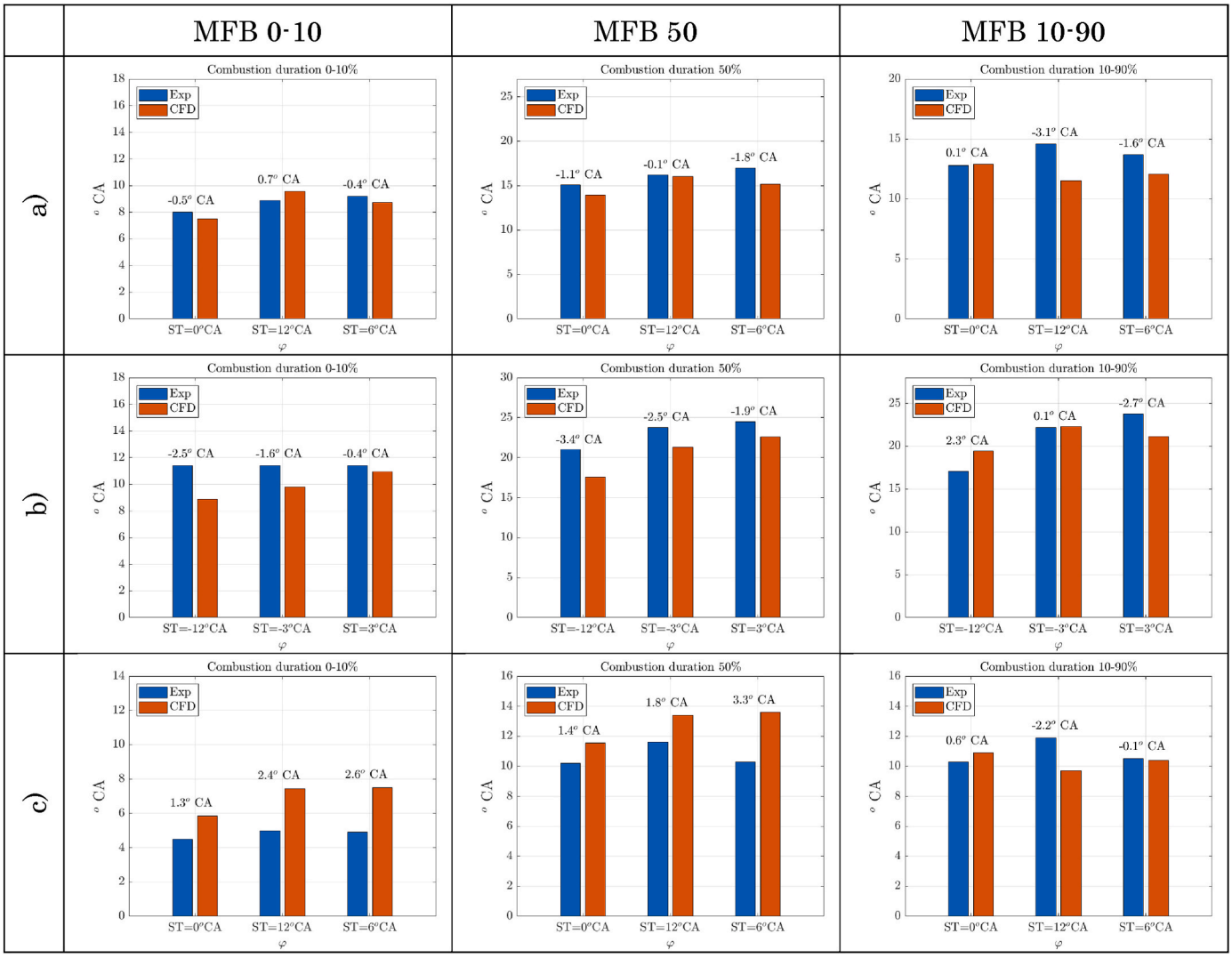

Fig. 8. Comparison between measured and computed combustion indicators for a) 2000 rpm - $\varphi = 0.8$ case, b) 3000 rpm - $\varphi = 0.6$ case and c) 3000 rpm - $\varphi = 0.8$ case.

determination R^2 and the pressure peak percentage error are also reported. The worst errors can be noticed in the 3000 rpm - φ = 0.8 sweep, especially for the more advanced spark times. Conversely, the best results are observed in the φ = 0.6 sweep. A possible explanation is related to the injection duration. The longer it is, the lower the time for the mixing becomes. In turn, the mixing dampens (by homogenizing) potential errors due to, for example, inaccuracies in the injection modeling. In this regard, the 3000 rpm - φ = 0.8 sweep is the one characterized by the lowest time intervals between injection end and ST.

In order to strengthen the validation of the numerical methodology, Fig. 8 reports the combustion indicators MFB 0–10, MFB 50 and MFB 10–90 (duration), for all the cases. The absolute errors are also reported in figure, ranging from −3.4° CA up to +3.3° CA. Although these errors highlight the limits of the numerical methodology (opening to the possibility of improvements), the considerable number of cases as well as the absence of case-to-case tuning allow to consider the setup as adequate to predict combustion. Therefore, the attention can be focused on the validation of the predictive capabilities of the model about the NO_x emissions.

In this regard, Fig. 9a) to 9c) show the comparison between CFD and experiments in terms of NO_x. In the first column, such a comparison is carried out for all the investigated cases. The second column shows the prediction errors by the simulations, including the average values for each sweep. Moreover, on the numerical side, two different sets of results are presented, one per tested chemical scheme. It is important to point out that the numerical NO_x quantities reported in Fig. 9a) to 9c) correspond to the sums of NO and NO_2 and they are the mg present at the exhaust valve opening. Therefore, it is supposed that reactions are

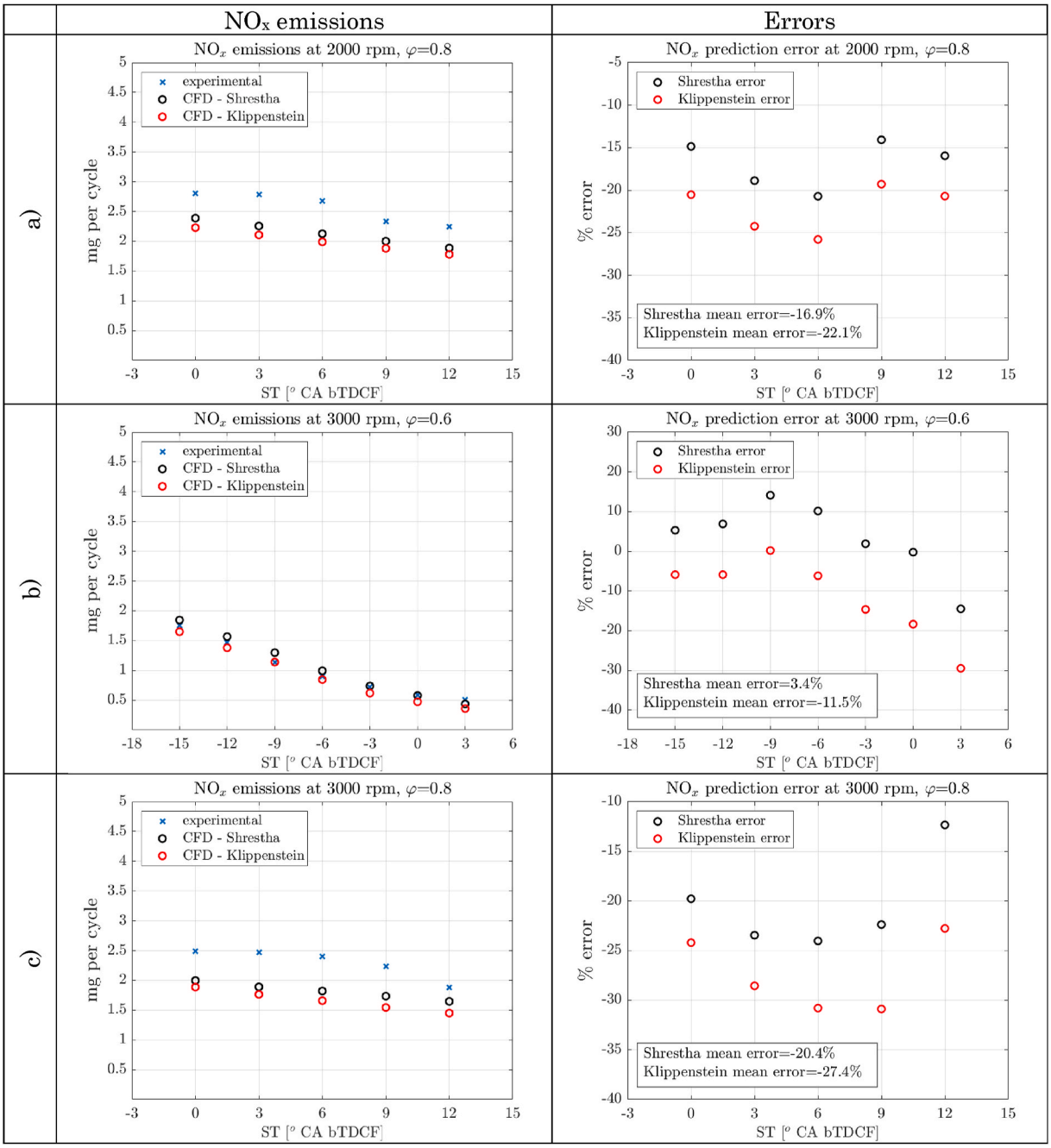

Fig. 9. Numerical and experimental NO_x emissions as a function of the spark time for a) 2000 rpm - φ = 0.8 case, b) 3000 rpm - φ = 0.6 case and c) 3000 rpm - φ = 0.8 case.

frozen in the exhaust pipe, following the validated practice proposed in Ref. [34]. NO and NO_2 mass fractions are not separately presented as, for all the cases, NO_2 mass fraction is always at least 4 orders of magnitude lower than NO mass fraction.

The simulations are able to match qualitatively and quantitatively the experimental data. Firstly, for all the revving speeds and the equivalence ratios, numerical results are able to properly reproduce the trend as a function of the spark time. In addition, focusing on $\varphi = 0.8$ cases, the decrease of NO_x increasing the revving speed is properly captured by the simulations. Similarly, on equal revving speed (3000 rpm), CFD is able to correctly predict an increase of NO_x with the equivalence ratio. Moreover, in quantitative terms, all the numerical data are very close to the experimental counterparts, which means all the involved phenomena, gas injection, mixing, combustion and chemical reactions are reasonably captured by the proposed CFD methodology. As for the chemistry, it is interesting to point out that, despite the mechanism by Shrestha always provides slightly better estimations compared to the one by Klippenstein, the two mechanisms provide similar results. This is a proof that NO_x emissions can be properly estimated regardless the mechanism, provided that the latter is well validated (as the adopted ones). Moreover, considering Shrestha mechanism, although the errors seem to be relevant (with values even greater than 20%), they are in line with the values proposed in other publications [17–20]. Reducing the error in NO_x prediction is not trivial, as many factors concur in the determination of the emissions. In other words, it is necessary to be confident on the modelling of several phenomena to have accurate predictions of the nitrogen oxides, such as turbulence, hydrogen gas injection, mixing, combustion and chemical reactions in the burnt gases. It must be noted that, for specific aspects, errors are consciously accepted. For example, the DC model requires a detailed mechanism accurately describing all the reactions that can occur. However, this would lead to the adoption of mechanisms containing lot of species and reactions. In order to speed up the simulations and keep the computational time acceptable, reduced or skeletal mechanisms are usually preferred, which are inevitably characterized by lower accuracy compared to the detailed versions.

Before the result discussion, a brief deepening on the impact of the computational grid on NO emissions is proposed. Compared to the grid ("coarse") adopted for the previously presented analyses, a finer version ("fine") is built by halving the cell size in the core of the domain. The new mesh is characterized by 2.3 M cells, which is roughly six times the cell number of the base one. Fig. 10a) and 10b) show the comparisons in terms of in-cylinder pressure and NO mass between "coarse" and "fine" grids (only in one of the investigated cases, for brevity). Despite the considerable modification of the grid, negligible differences can be noticed in the results. In fact, pressure peak and NO mass at the end of the cycle vary of +2% and +0.24%, respectively. This means that the coarse grid is already sufficiently fine to achieve grid-independence. As previously discussed, NO concentration is orders of magnitude higher than the NO_2 one. For this reason, the comparison in Fig. 10b) only refers to NO.

4.2. Discussion of the results

Once the model is validated, the results are discussed in the following to highlight the effect on NO_x emissions of two engine parameters, namely spark and injection timings. They affect in-cylinder temperature and mixture stratification, respectively, which are widely recognized to dominate formation of nitrogen oxides. It is useful to point out that such analysis not only aims to understand the phenomena leading to emission formation, but it tries to emphasize the potential of the CFD to deeply investigate such phenomena. This (along with the proven predictive capabilities) makes the use of CFD suitable for the optimization of the engine parameters to lower the emissions and simultaneously preserve the performance.

4.2.1. Effect of the spark timing

Decreasing the spark advance leads to a reduction of the maximum pressure inside the cylinder. The reason is that the heat release rate occurs later and later in the cycle, and it is less and less able to compensate the decrease of pressure as a consequence of the cylinder volume increase. Similarly to the pressure behavior, the maximum temperature of the exhaust gases decreases as well. In this regard, Fig. 11a) and 11 b) show in-cylinder pressures and temperatures for the sweep at 3000 rpm and $\varphi = 0.8$. Since in this case the leading mechanism for NO_x formation is the thermal one, the consequence of a temperature reduction is a lower formation of NO_x, as visible in Fig. 9c). It is useful to point out that, for brevity, only the condition at 3000 rpm and $\varphi = 0.8$ is considered for the present analysis, but the same trends and considerations are valid for the other operating conditions. It is interesting to observe in Fig. 11 that, reducing the spark advance, despite a strong peak pressure drop, the average temperature in the cylinder shows a minimal decrease of the peak (equal to −26 K) between the extremal cases. This is the reason why, advancing the spark timing (i.e. delaying the combustion), the NO_x decrease is poor.

4.2.2. Effect of the injection timing

NO_x emissions are not simply related to the mean mixture quality, but they are strongly dependent on the local stratification. This is confirmed by the proposed simulations. For example, focusing on the 3000 rpm cases, Fig. 12a) to 12f) show temperature, equivalence ratio and NO mass fraction for two different cases, one at $\varphi = 0.6$ and one at φ

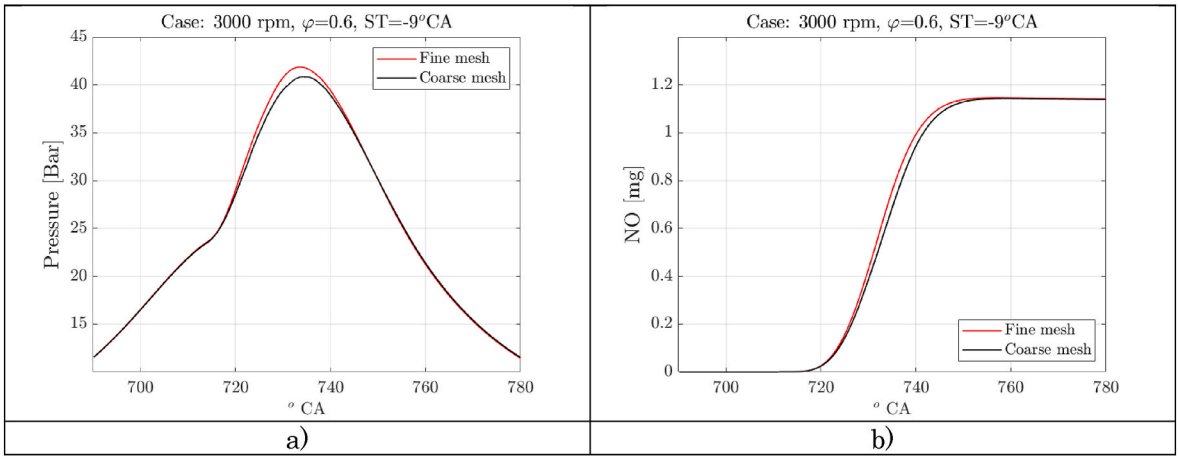

Fig. 10. Comparison in terms of a) pressure and b) NO mass between coarse and fine grids.

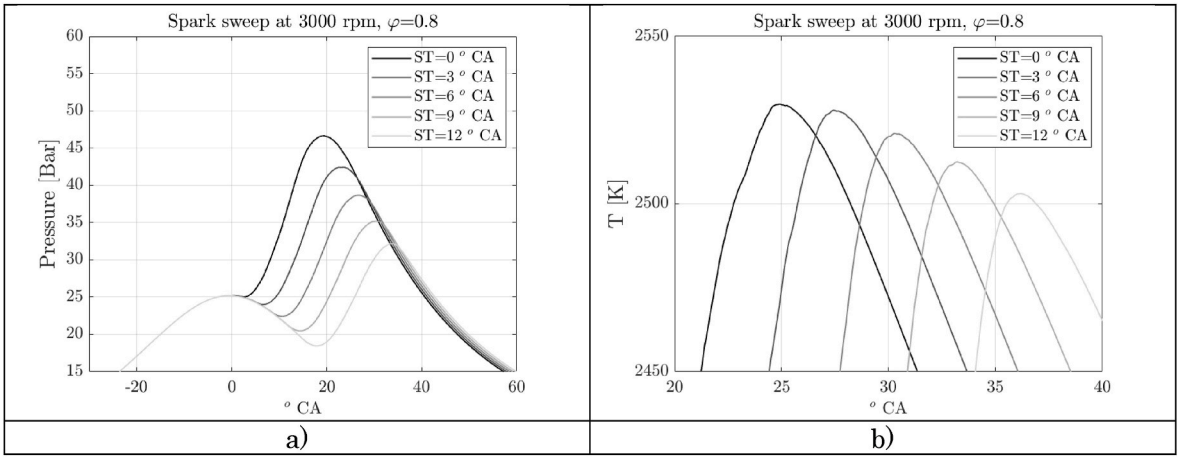

Fig. 11. Computed in-cylinder pressures a) and temperatures b) for the different spark times at 3000 rpm and φ = 0.8.

= 0.8 (further details on the proposed images can be found in the caption). Only NO is considered in the following, as the concentration of NO_2 is negligible in comparison. Looking at the φ = 0.6 case, temperature seems to be the main promoter of NO formation as the highest concentration values are roughly located in correspondence of the highest temperature region. Although T is unquestionably a leading factor for nitrogen oxides formation, the main responsible of the local peak is actually the local φ, which is close to 0.8. As a demonstration, it is possible to observe in Fig. 12d) to 12f) the results of the φ = 0.8 case, where the high values of NO concentration do not correspond to the ones of T but, rather, to the presence of local mixture at φ ∼ 0.8. Such an outcome is confirmed in literature by the works of Hairong [19] and Duan [68].

To understand the importance of an equivalence ratio equal (or close) to 0.8, 1D chemical kinetics computations of freely propagating flame are carried out using DARS. A single mechanism is considered for brevity in this analysis, i.e. the one by Shrestha. Pressure and unburnt temperature profiles adopted for the computations are representative of the in-cylinder conditions for the analyzed operations and they are provided by the 3D-CFD. Fig. 13 shows the NO mass fraction from 1D simulations at fixed pressure and unburnt temperature (40 bar and 900 K). Other conditions are omitted as the qualitative behavior with respect

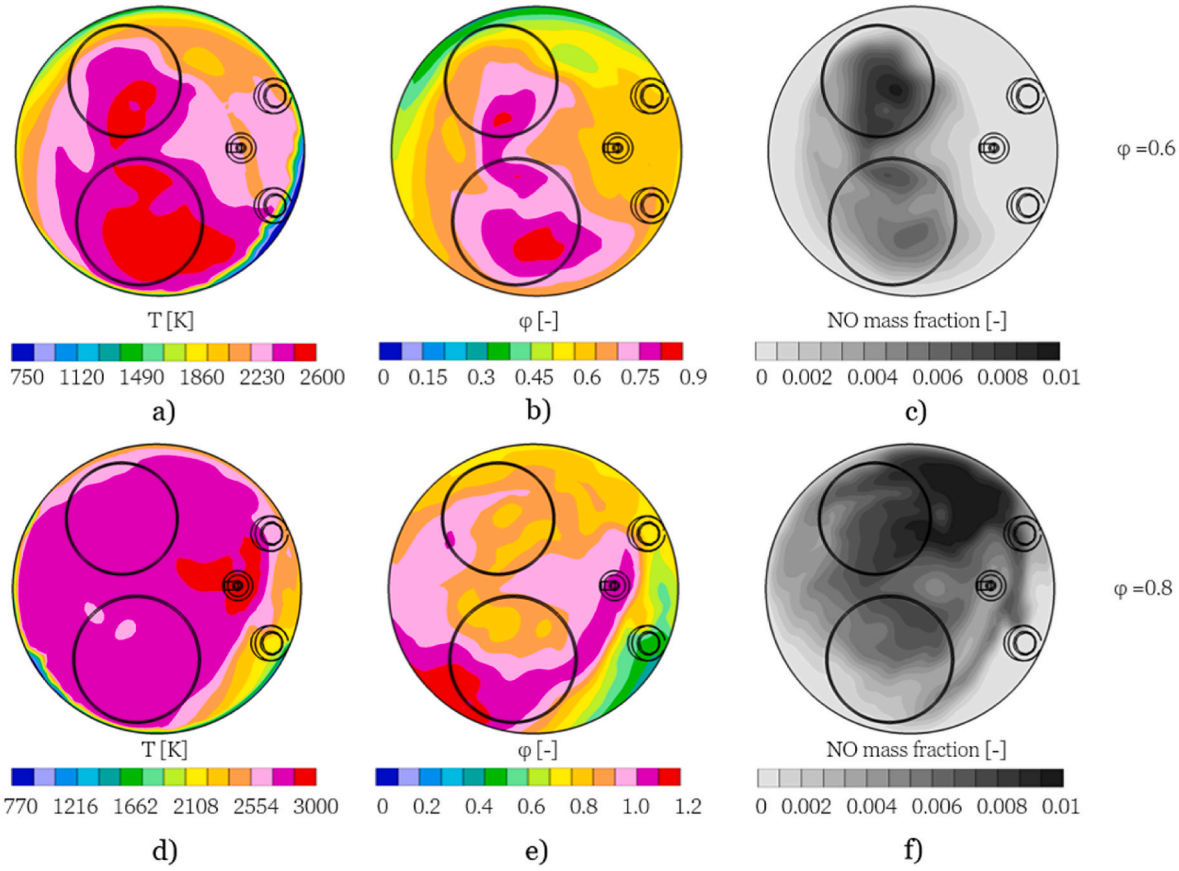

Fig. 12. a), b) and c) show temperature, equivalence ratio and NO mass fraction at 750°CA for the case 3000 rpm, φ = 0.8 and ST = −15°CA; d), e) and f) report the same quantities at 740°CA for the case 3000 rpm, φ = 0.6 and ST = 0°CA on a section distant 5 mm from head plane.

to φ is marginally affected by p or T. The methodology to extract NO mass fractions from freely propagating flame computations is presented in Ref. [22]. Similarly to the 3D analyses, the attention is focused on NO as the other nitrogen oxides are characterized by remarkably lower concentrations. Interestingly, Fig. 13 shows that NO production increases with the equivalence ratio up to φ ∼ 0.8. Then it rapidly decreases so that, at stoichiometry, the NO mass fraction is nearly the same as that at φ ∼ 0.45.

In the light of this result, on the one hand, it is possible to relate the peak of NO to local φ close to 0.8, in agreement with the outcomes of the 3D simulations. On the other hand, still considering the in-cylinder analyses, it is possible to conclude that, for the φ = 0.8 case, increasing the mixture homogeneity is counterproductive. In fact, the peak of NO is positioned where the local φ is close to the average value. Pockets that are richer and leaner compared to the average value are characterized by lower NO mass fraction, as observed in Fig. 12. A further confirmation of the mixture stratification importance comes from the adiabatic flame temperature reported in Fig. 14 as function of φ. The plot still refers to 40 bar and 900 K and only one condition is considered, for the same reasons previously commented. The peak of adiabatic flame T is reached at equivalence ratio of nearly 1.1, thus for slightly rich mixtures. Considering the importance of T for NO_x formation, Fig. 14 would suggest a peak of NO at φ close to 1.1. Instead, Fig. 13 shows a peak at φ ∼ 0.8. The reason is that, moving from φ ∼ 0.8 to φ ∼ 1.1, the oxygen becomes insufficient to both complete the H_2 oxidation and generate NO_x. In this situation, since the oxidation process of the hydrogen is faster than the one of nitrogen, NO production drastically reduces even if the temperature increases. This confirms the role of φ. The impact of the φ variation overcomes the temperature effect, although T is of primary importance here, as the main mechanism of NO_x formation is the thermal one.

Once the impact of the mixture stratification on nitrogen oxides formation is clear, it is important to emphasize that one of the main responsible of the resulting local φ is the injection timing. As a demonstration, a delayed start of injection (SOI) is simulated, which allows less time for the H_2 to mix with air. This leads to a lower mixture homogeneity at spark time. At 3000 rpm, the time window available for the injection is too short to account for a shift of the injection law. Therefore, the point at φ = 0.8 and 2000 rpm is considered. In particular, the ST = 0° CA is selected as reference for the SOI sensitivity. The original SOI is equal to 175°CA bTDCF and it is an optimized injection timing determined by the experimental tests. Details on this can be found in Ref. [27]. The new value is equal to 150°CA bTDCF and it implies a shift towards the TDCF. The value is purposely selected so that,

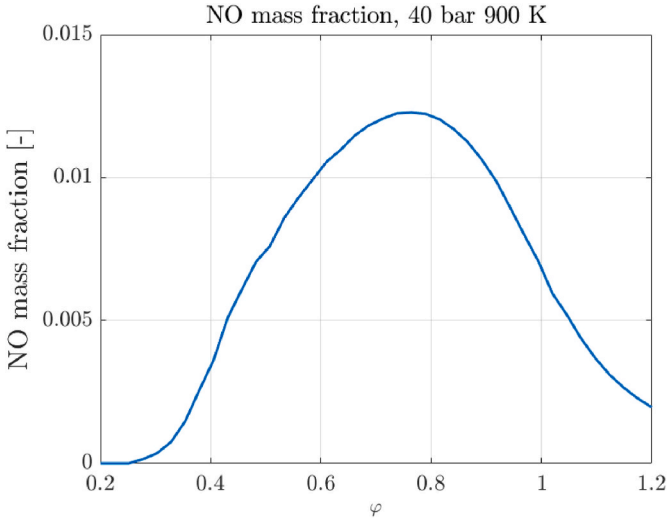

Fig. 13. NO mass fraction as a function of the equivalence ratio.

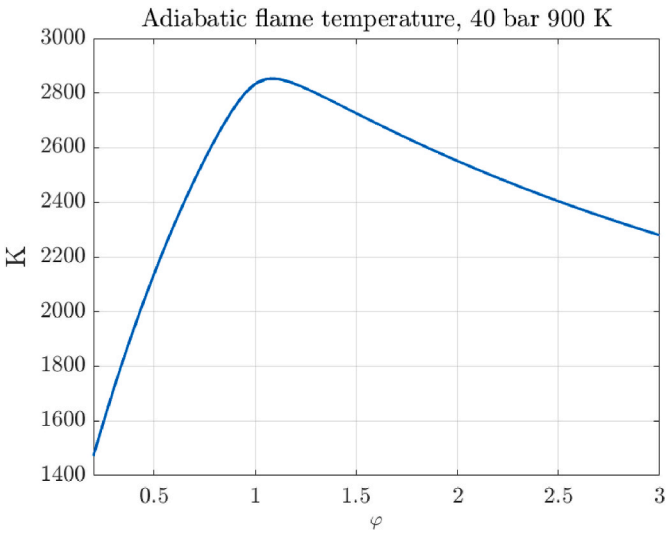

Fig. 14. Adiabatic flame temperature at 40 bar and 900 K.

similarly to the original case, the injection occurs under sonic condition of the injector. In this regard, Fig. 15 reports the two injection laws, the dimensionless intake valve lift (as a reference) and the critical pressure above which the injectors start to operate in subcritical conditions. Such critical value is computed as in Eq. (10):

$$p_{crit} = p_{inlet}\left(\frac{2}{\gamma+1}\right)^{\frac{\gamma}{\gamma-1}} \tag{10}$$

p_{inlet} is the injector feeding pressure and γ the specific heat ratio of hydrogen. Although the delayed injection law is translated by 25° CA, the injector still operates at sonic conditions for the whole event as the injection ends well before the in-cylinder pressure overcomes the critical value. This is important as the injection parameters (in particular hydrogen velocity and mass flow rate) remain the same while the phasing changes.

As visible in Fig. 16, which shows the probability density function (PDF) of φ across the computational domain at the spark time, the mixture homogeneity worsens significantly by delaying the injection. This leads, in turn, to a reduction of NO mass of 17.1%, as shown in Fig. 17a). In other words, the delayed injection law (starting at 150°CA bTDCF) leads to a more heterogeneous mixture, which counterintuitively reduces the NO_x emissions by approximately 17.1% compared to

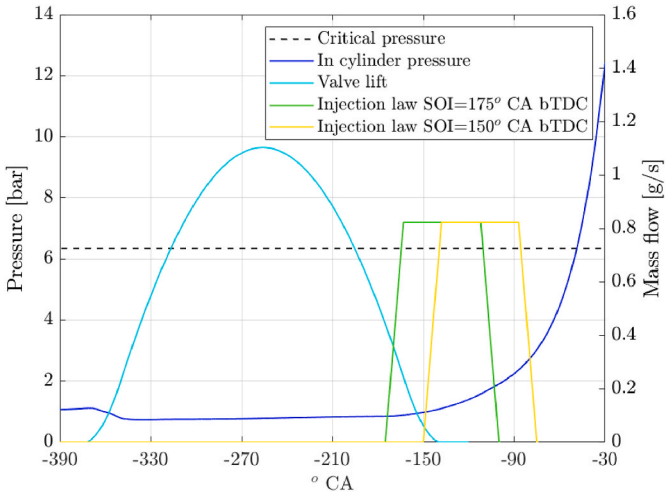

Fig. 15. Intake valve lift (non dimensional), cylinder pressure, critical pressure and injection laws for the case at 2000 rpm, φ = 0.8 and ST = 0°CA.

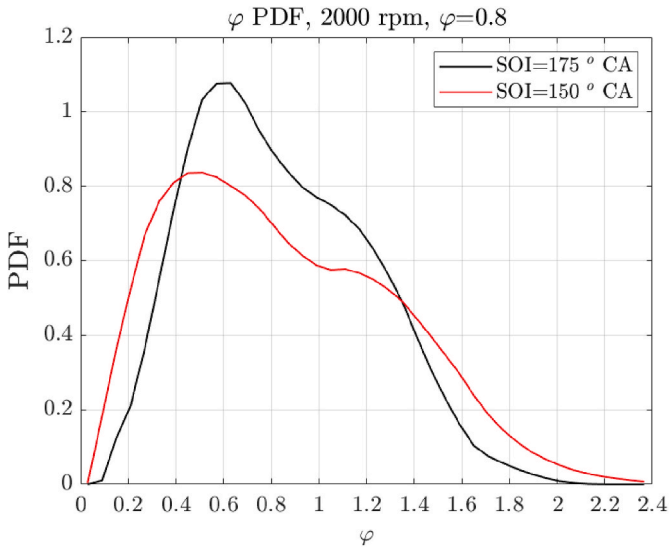

Fig. 16. Probability density function of φ at 2000 rpm, φ = 0.8 and ST = 0° CA, for two different SOI, namely 175°CA bTDCF and 150°CA bTDCF.

the earlier injection law (starting at 175°CA bTDCF). This is coherent with the above, that is reducing the homogeneity of a mixture whose average φ is (roughly) the one of maximum NO production is beneficial.

It is important to point out that the case with the new injection law provides a higher performance, thanks to both a slight improvement of the volumetric efficiency (due to a smaller overlap between the openings of intake valve and injector) and a richer mixture around the spark (which is beneficial in terms of ignition). Therefore, for a fair comparison, the NO emissions are also shown normalized by the power output, in Fig. 17b). Even in this case, the reduction of NO is confirmed.

Interestingly, the proposed numerical sensitivity to the SOI is confirmed by experimental evidences existing in literature. In fact, Kim et al. [69] test different injection timings and show that a delay of the SOI leads to a reduction of the NO_x emissions.

Moreover, although in the present analysis the attention is focused on the effect of the SOI, also the injection pressure strongly affects NO_x emissions. As shown by Huang et al. [70], decreasing the injection pressure has the same effect as the SOI delay. In fact, lower pressure means (on equal injected mass) longer injection duration and, thus, an injection closer and closer to the TDC, with a consequent increase of the mixture stratification.

5. Conclusions

In the present paper, a 3D-CFD methodology for in-cylinder simulations is proposed and validated against experimental data. The numerical methodology aims at predicting both performance and NO_x formation in case of H_2 combustion. It relies on in-house developed models for ignition and heat transfer. As for combustion, the G-Equation model is adopted, which is based on a Damköhler-derived turbulent flame speed correlation and the well-consolidated laminar flame speed by Verhelst. NO_x emissions in the burnt gases are simulated using detailed chemistry approach relying on validated chemical mechanisms.

The investigated engine is a single cylinder Diesel converted to spark-ignition hydrogen combustion by the addition of spark-plug and two low pressure gas injectors. Different revving speeds and mixture qualities are considered for the numerical analyses and, for each condition, multiple spark times are simulated. The methodology proves to reliably estimate both in-cylinder pressure and NO_x emissions, at the different investigated operating points, with no case-by-case adaptation of the model constants.

A deeper analysis of the CFD results points out the impact of spark and injection timings, which in turn affect temperature and mixture stratification and, thus, NO_x formation. In particular, a spark advance reduction leads to a decrease of both in-cylinder pressure and temperature. However, while NO_x emissions are just slightly reduced (as the temperature peak is scarcely influenced by the spark timing), pressure is strongly sensitive and this leads to a considerable drop of both performance and efficiency of the engine. As for the mixture stratification, 1D chemical kinetics simulations indicate φ ∼ 0.8 as the most critical one for NO_x emissions. 3D results confirm that NO_x mass fraction is strongly higher where the local equivalence ratio of the mixture inside the chamber is equal (or close) to 0.8. Moreover, it is demonstrated that, in case of combustion of a mixture with average φ equal to 0.8, the greater the mixture homogeneity is (thanks to an injection timing advance), the higher the NO_x concentration at the exhaust becomes. The capabilities of the 3D-CFD numerical methodology to predict NO_x emissions and deepen the phenomena leading to their formation make the methodology suitable to be adopted in the optimization of engine parameters (such as spark and injection timings), with the aim to reduce tailpipe emissions and simultaneously preserve the performance.

It is finally fair to discuss the limitations of the proposed 3D-CFD methodology, that can also be considered as hints for possible future developments. The limitations are mainly related to the validation. For example, the absence of gas injection experiments is one of the most critical aspects. In fact, mixture stratification (which strictly depends on the injection process) is one of the main drivers of the NO_x formation, as widely discussed in the text. Although in this work there is no rigorous

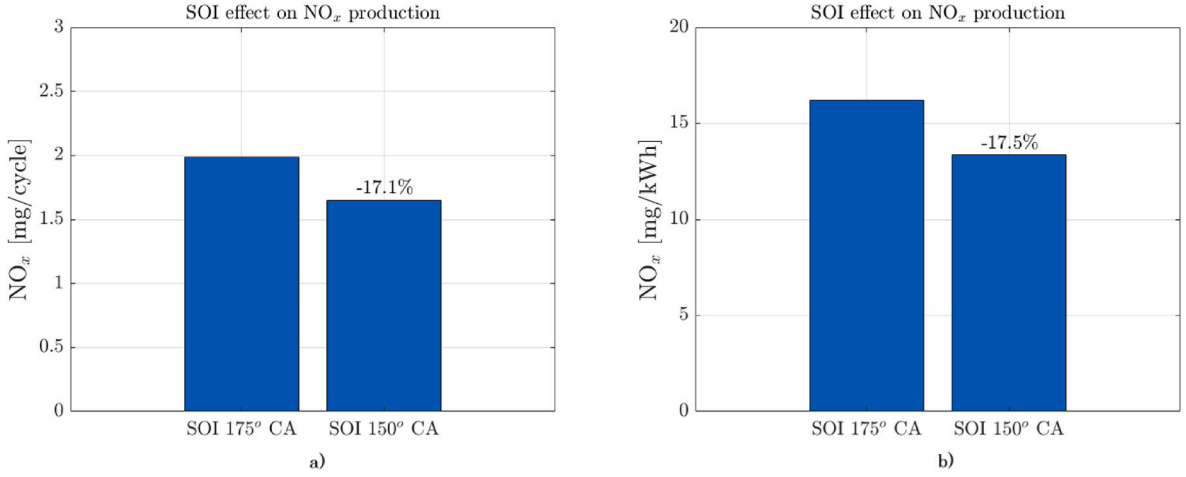

Fig. 17. NO_x emission variation with SOI at 2000 rpm and φ = 0.8; a) shows values in mg/cycle, while b) in mg/kWh.

validation in terms of H_2 jets, the agreement obtained with in-cylinder pressure and NO_x emissions is a sort of indirect proof of a reasonable representation of the injection. Still in terms of validation, the range of operating conditions should be further expanded to include lower and higher engine speeds as well as other equivalence ratios (both leaner and richer). Another potential limitation is the flame thermo-diffusive instability effect which is completely neglected in this work. Some of these aspects are already under investigation by the authors and they will be object of future works.

CRediT authorship contribution statement

Stefano Sfriso: Writing – original draft, Investigation, Formal analysis. **Fabio Berni:** Writing – review & editing, Supervision, Methodology, Conceptualization. **Stefano Fontanesi:** Writing – review & editing, Supervision, Project administration, Conceptualization. **Alessandro d'Adamo:** Writing – review & editing, Methodology, Conceptualization. **Sebastiano Breda:** Writing – review & editing, Methodology, Conceptualization. **Luigi Teodosio:** Writing – review & editing, Conceptualization. **Stefano Frigo:** Writing – review & editing, Resources, Methodology, Investigation, Data curation. **Marco Antonelli:** Writing – review & editing, Validation, Methodology, Investigation, Data curation.

Declaration of competing interest

The authors declare that they have no known competing financial interests or personal relationships that could have appeared to influence the work reported in this paper.

Acknowledgments

The experimental work described in this paper has been conducted by Marco Antonelli and Luigi Martorano from the University of Pisa, in a regional project named 'H2-Filiera idrogeno' promoted by Tuscany.

The authors gratefully acknowledge the University of Modena and Reggio Emilia for supporting the activity by the "Fondo di Ateneo per la Ricerca 2024 per il finanziamento di piani di sviluppo dipartimentale nell'ambito della ricerca" (FARD 2024–2025) and the "PIANO NAZIONALE DI RIPRESA E RESILIENZA (PNRR) – MISSIONE 4 COMPONENTE 2, "Dalla ricerca all'impresa" INVESTIMENTO 1.4, Potenziamento strutture di ricerca e creazione di "campioni nazionali di R&S" su alcune Key Enabling Technologies, finanziato dall'Unione europea – NextGenerationEU - Progetto identificato con codice CN00000023. Titolo "Sustainable Mobility Center (Centro Nazionale per la Mobilità Sostenibile – CNMS)" - Spoke 12 - Avviso MUR 3138/2021 modificato con DD 3175/2021".

SYMBOLS/ABBREVIATIONS

A	Turbulent flame speed model constant
A_k	Flame kernel surface
aTDC(F)	after Top Dead Center (of Firing)
BDC	Bottom Dead Center
bTDC(F)	before Top Dead Center (of Firing)
c	Regress variable
C_p	Specific heat at constant pressure
CA	Crank Angle
CFD	Computational Fluid Dynamics
CI	Compression Ignition
CR	Compression Ratio
d_{gap}	Distance between spark electrodes
DC	Detailed Chemistry
ECFM	Extended Coherent Flamelet Model
ECU	Engine Control Unit
EGR	Exhaust Gases Recirculation
$F_{i,j}$	Diffusion flux component
G	Passive flame propagation scalar
ICE	Internal Combustion Engine
k	Thermal conductivity
k_{fR}	Forward reaction R rate constant
k_{rR}	Backward reaction R rate constant
LES	Large Eddy Simulation
LFS	Laminar flame speed
M_i	Molar weight of species *i*
MFB	Mass of Fuel Burnt
NO_x	Nitorgen Oxides
P	Pressure
p_{crit}	Critical pressure
PDF	Probability Density Function
p_{inlet}	Inlet pressure
r_k	Flame kernel radius
$r_{k,init}$	Initial condition for flame kernel radius
$[R_k]$	Mole concentration of element R_k
RANS	Reynold Average Navier Stokes
rpm	Revolution Per Minute
S_i	Production/consumption rate for species *i*
S_L	Laminar flame speed
S_T	Turbulent flame speed
S_{plasma}	Expansion velocity of plasma channel
SI	Spark Ignition
SOI	Start Of Injection
ST	Spark Time
T	Temperature
t	Time

(*continued on next page*)

(*continued*)

TDC(F)	Top Dead Center (of Firing)
$\mathbf{T_k}$	Flame kernel temperature
URANS	Unsteady Reynold Average Navier Stokes
$\mathbf{V_k}$	Flame kernel volume
$\mathbf{V_{k,init}}$	Initial condition for flame kernel volume
u'	Velocity fluctuations RMS
$\mathbf{u_i}$	i-th velocity component
x	Space coordinate
$\mathbf{Y_i}$	Mass fraction of species *i*
$\boldsymbol{\delta_L}$	Laminar flame thickness
$\boldsymbol{\varphi}$	Equivalence ratio
$\boldsymbol{\gamma}$	Specific heats ratio
ν'_{Ri}	Stoichiometric coefficient of reactant species *i* in reaction R
ν''_{Ri}	Stoichiometric coefficient of product species *i* in reaction R
$\boldsymbol{\rho_k}$	Flame kernel density
$\boldsymbol{\rho}$	Density
$\boldsymbol{\rho_u}$	Unburnt density

References

[1] Valdés M, Abbas R, Rovira A, Martín-Aragón J. Thermal efficiency of direct, inverse and sCO 2 gas turbine cycles intended for small power plants. Energy. Apr. 2016;100:66–72. https://doi.org/10.1016/j.energy.2016.01.072.

[2] De Paepe W, Montero Carrero M, Bram S, Parente A, Contino F. Toward higher micro gas turbine efficiency and flexibility—humidified micro gas turbines: a review. J Eng Gas Turbines Power Aug. 2018;140(8). https://doi.org/10.1115/1.4038365.

[3] Stępień Z. A comprehensive overview of hydrogen-fueled internal combustion engines: achievements and future challenges. MDPI; Oct. 01, 2021. https://doi.org/10.3390/en14206504.

[4] Mazloomi K, Gomes C. Hydrogen as an energy carrier: prospects and challenges. Jun. 2012. https://doi.org/10.1016/j.rser.2012.02.028.

[5] Winkelmann J. Diffusion of hydrogen (1); air (2). 2007. p. 1309. https://doi.org/10.1007/978-3-540-49718-9_986. 1309.

[6] Matalon M. The Darrieus-Landau instability of premixed flames. Fluid Dynam Res Aug. 2018;50(5). https://doi.org/10.1088/1873-7005/aab510.

[7] Chand P, kumar Hod M. Hydrogen fueled I.C. Engine [Online]. Available: http://ijesc.org/; 2017.

[8] Verhelst S, Sierens R. Hydrogen engine-specific properties [Online], www.elsevier.com/locate/ijhydene; 2001.

[9] Fogla N, Creta F, Matalon M. Effect of folds and pockets on the topology and propagation of premixed turbulent flames. Combust Flame Jul. 2015;162(7):2758–77. https://doi.org/10.1016/j.combustflame.2015.04.012.

[10] Al-Shahrany AS, Bradley D, Lawes M, Liu K, Woolley R. DARRIEUS–LANDAU and thermo-acoustic instabilities in closed vessel explosions. Combust Sci Technol Dec. 2006;178(10–11):1771–802. https://doi.org/10.1080/00102200600788734.

[11] Bradley D, Lawes M, Liu K, Mansour MS. Measurements and correlations of turbulent burning velocities over wide ranges of fuels and elevated pressures. Proc Combust Inst 2013;34(1):1519–26. https://doi.org/10.1016/j.proci.2012.06.060.

[12] Kalghatgi G, Head R, Chang J, Viollet Y, Babiker H, Amer A. An alternative method based on toluene/n-heptane surrogate fuels for rating the anti-knock quality of practical gasolines. Int J Franch Law 2014;7(3):663–72. https://doi.org/10.2307/26273706.

[13] Dhyani V, Subramanian KA. Experimental investigation on effects of knocking on backfire and its control in a hydrogen fueled spark ignition engine. Int J Hydrogen Energy Apr. 2018;43(14):7169–78. https://doi.org/10.1016/J.IJHYDENE.2018.02.125.

[14] Yang R, Liu Z, Liu J. The methodology of decoupling fuel and thermal nitrogen oxides in multi-dimensional computational fluid dynamics combustion simulation of ammonia-hydrogen spark ignition engines. Int J Hydrogen Energy Feb. 2024;55:300–18. https://doi.org/10.1016/j.ijhydene.2023.09.105.

[15] Yan Y, Shang T, Li L, Liu Z, Liu J. Assessing hydrogen–ammonia ratios to achieve rapid kernel inception in spark-ignition engines. J Energy Resour Technol Jun. 2024;146(6). https://doi.org/10.1115/1.4065198.

[16] Liu J, Liu Z. In-cylinder thermochemical fuel reforming for high efficiency in ammonia spark-ignited engines through hydrogen generation from fuel-rich operations. Int J Hydrogen Energy Feb. 2024;54:837–48. https://doi.org/10.1016/j.ijhydene.2023.08.146.

[17] Rakopoulos CD, Kosmadakis GM, Demuynck J, De Paepe M, Verhelst S. A combined experimental and numerical study of thermal processes, performance and nitric oxide emissions in a hydrogen-fueled spark-ignition engine. Int J Hydrogen Energy Apr. 2011;36(8):5163–80. https://doi.org/10.1016/j.ijhydene.2011.01.103.

[18] Kosmadakis GM, Rakopoulos CD, Demuynck J, De Paepe M, Verhelst S. CFD modeling and experimental study of combustion and nitric oxide emissions in hydrogen-fueled spark-ignition engine operating in a very wide range of EGR rates. Int J Hydrogen Energy Jul. 2012;37(14):10917–34. https://doi.org/10.1016/j.ijhydene.2012.04.067.

[19] Zhu H, Duan J. Research on emission characteristics of hydrogen fuel internal combustion engine based on more detailed mechanism. Int J Hydrogen Energy Feb. 2019;44(11):5592–8. https://doi.org/10.1016/j.ijhydene.2018.08.044.

[20] Lu C, et al. Numerical investigation on gaseous fuel injection strategies on combustion characteristics and NO emission performance in a pure hydrogen engine. Fuel May 2024;363:130911. https://doi.org/10.1016/J.FUEL.2024.130911.

[21] Maio G, et al. Experimental and numerical investigation of a direct injection spark ignition hydrogen engine for heavy-duty applications. Int J Hydrogen Energy Aug. 2022;47(67):29069–84. https://doi.org/10.1016/j.ijhydene.2022.06.184.

[22] Berni F, Pessina V, Teodosio L, d'Adamo A, Borghi M, Fontanesi S. An integrated 0D/1D/3D numerical framework to predict performance, emissions, knock and heat transfer in ICEs fueled with NH3–H2 mixtures: the conversion of a marine Diesel engine as case study. Int J Hydrogen Energy Oct. 2023. https://doi.org/10.1016/j.ijhydene.2023.09.158.

[23] Liang L, Reitz RD. Spark ignition engine combustion modeling using a level set method with detailed chemistry. Apr. 2006. https://doi.org/10.4271/2006-01-0243.

[24] Yang S, Reitz RD, Iyer CO, Yi J. Improvements to combustion models for modeling spark-ignition engines using the G-equation and detailed chemical kinetics. SAE Int J Fuels Lubr Jun. 2008;1(1). https://doi.org/10.4271/2008-01-1634. 2008-01–1634.

[25] Sfriso S, et al. Proposal and validation of a numerical framework for 3D-CFD in-cylinder simulations of hydrogen spark-ignition internal combustion engines. Int J Hydrogen Energy Jan. 2024;53:114–30. https://doi.org/10.1016/j.ijhydene.2023.12.027.

[26] Antonelli M, Martorano L. Realization and testing of a low pressure hydrogen direct injection engine using commercial injectors. In: *SAE technical papers*, SAE international; 2012. https://doi.org/10.4271/2012-01-0652.

[27] Simi A. Hydrogen direct injection in recirpocating engines using commercial injectors. PhD Dissertation; 2011.

[28] Yakhot V, Orszag S sA. Renormalization group analysis of turbulence. I. Basic theory. J Sci Comput 1986;1(1):3–51. https://doi.org/10.1007/BF01061452.

[29] STAR-CD methodology guide.

[30] Teodosio L, Berni F. Optimization via genetic algorithm of a variable-valve-actuation spark-ignition engine based on the integration between 1D/3D simulation codes and optimizer. Int J Engine Res 2022. https://doi.org/10.1177/14680874221099874.

[31] Berni F, et al. A zonal secondary break-up model for 3D-CFD simulations of GDI sprays. Fuel 2022;309(Feb). https://doi.org/10.1016/j.fuel.2021.122064.

[32] Iacovano C, Berni F, Barbato A, Fontanesi S. A preliminary 1D-3D analysis of the darmstadt research engine under motored condition. In: E3S web of conferences. EDP Sciences; Oct. 2020. https://doi.org/10.1051/e3sconf/202019706006.

[33] Sparacino S, Berni F, Riccardi M, Cavicchi A, Postrioti L. 3D-CFD simulation of a GDI injector under standard and flashing conditions. In: E3S web of conferences. EDP Sciences; Oct. 2020. https://doi.org/10.1051/e3sconf/202019706002.

[34] Berni F, et al. Modeling of gaseous emissions and soot in 3D-CFD in-cylinder simulations of spark-ignition engines: a methodology to correlate numerical results and experimental data. Int J Engine Res 2022. https://doi.org/10.1177/14680874221112564.

[35] Sfriso S, Berni F, Fontanesi S, D'Adamo A, Antonelli M, Frigo S. A 3D-CFD numerical approach for combustion simulations of spark ignition engines fuelled with hydrogen: a preliminary analysis. Apr. 2023. https://doi.org/10.4271/2023-01-0207.

[36] Berni F, Cicalese G, Borghi M, Fontanesi S. Towards grid-independent 3D-CFD wall-function-based heat transfer models for complex industrial flows with focus on in-cylinder simulations. Appl Therm Eng May 2021;190. https://doi.org/10.1016/j.applthermaleng.2021.116838.

[37] Berni F, Fontanesi S. A 3D-CFD methodology to investigate boundary layers and assess the applicability of wall functions in actual industrial problems: a focus on

in-cylinder simulations. Appl Therm Eng 2020;174(Jun). https://doi.org/10.1016/j.applthermaleng.2020.115320.
[38] Berni F, Cicalese G, Sparacino S, Cantore G. On the existence of universal wall functions in in-cylinder simulations using a low-Reynolds RANS turbulence model. In: AIP conference proceedings. American Institute of Physics Inc.; Dec. 2019. https://doi.org/10.1063/1.5138752.
[39] Cicalese G, Berni F, Fontanesi S. Integrated in-cylinder/CHT methodology for the simulation of the engine thermal field: an application to high performance turbocharged DISI engines. SAE Int J Engines Apr. 2016;9(1):601–17. https://doi.org/10.4271/2016-01-0578.
[40] Berni F, Cicalese G, Fontanesi S. A modified thermal wall function for the estimation of gas-to-wall heat fluxes in CFD in-cylinder simulations of high performance spark-ignition engines. Appl Therm Eng 2017;115:1045–62. https://doi.org/10.1016/j.applthermaleng.2017.01.055.
[41] Cicalese G, Berni F, Fontanesi S, D'Adamo A, Andreoli E. A comprehensive CFD-CHT methodology for the characterization of a diesel engine: from the heat transfer prediction to the thermal field evaluation. In: *SAE technical papers*, SAE international; 2017. https://doi.org/10.4271/2017-01-2196.
[42] d'Adamo A, Iacovano C, Fontanesi S. Large-Eddy simulation of lean and ultra-lean combustion using advanced ignition modelling in a transparent combustion chamber engine. Appl Energy 2020;280(Dec). https://doi.org/10.1016/j.apenergy.2020.115949.
[43] D'Adamo A, Breda S, Cantore G. Large-eddy simulation of cycle-resolved knock in a turbocharged SI engine. In: Energy procedia. Elsevier Ltd; 2015. p. 45–50. https://doi.org/10.1016/j.egypro.2015.11.881.
[44] Lee M, Hall M, Ezekoye O, Matthews R. Voltage, and energy deposition characteristics of spark ignition systems. SAE technical papers. Apr. 2005. https://doi.org/10.4271/2005-01-0231.
[45] Huang S, Li T, Ma P, Xie S, Zhang Z, Chen R. Quantitative evaluation of the breakdown process of spark discharge for spark-ignition engines. J Phys D Appl Phys 2020;53(4):045501. https://doi.org/10.1088/1361-6463/ab56da.
[46] Stevens CR. Energy storage and the criteria for proper ignition in the internal combustion engine. IEEE Trans Ind Electron Control Instrum 1965;IECI-12(1):8–13. https://doi.org/10.1109/TIECI.1965.229542.
[47] Herweg R, Maly RR. A fundamental model for flame kernel formation in S. I. Engines. SAE Trans 1992;101:1947–76 [Online]. Available: http://www.jstor.org/stable/44611342.
[48] Trelles JP, Heberlein JVR, Pfender E. Non-equilibrium modelling of arc plasma torches. J Phys D Appl Phys Oct. 2007;40(19):5937–52. https://doi.org/10.1088/0022-3727/40/19/024.
[49] Trelles JP, Chazelas C, Vardelle A, Heberlein JVR. Arc plasma torch modeling. J Therm Spray Technol Dec. 2009;18(5–6):728–52. https://doi.org/10.1007/s11666-009-9342-1.
[50] Haidar J. Non-equilibrium modelling of transferred arcs. 1999.
[51] Gleizes A, Gonzalez JJ, Freton P. Thermal plasma modelling. May 07, 2005. https://doi.org/10.1088/0022-3727/38/9/R01.
[52] Lucchini T, et al. A comprehensive model to predict the initial stage of combustion in SI engines. Apr. 2013. https://doi.org/10.4271/2013-01-1087.
[53] Willems H, Sierens R. Modeling the initial growth of the plasma and flame kernel in SI engines. J Eng Gas Turbines Power Apr. 2003;125(2):479–84. https://doi.org/10.1115/1.1501912.
[54] Colin O, Truffin K. A spark ignition model for large eddy simulation based on an FSD transport equation (ISSIM-LES). Proc Combust Inst 2011;33(2):3097–104. https://doi.org/10.1016/j.proci.2010.07.023.
[55] Siemens PLM. DARS v2020.1 manual - book 2. 2020.
[56] Shrestha KP, Seidel L, Zeuch T, Mauss F. Detailed kinetic mechanism for the oxidation of ammonia including the formation and reduction of nitrogen oxides. Energy Fuels Oct. 2018;32(10):10202–17. https://doi.org/10.1021/acs.energyfuels.8b01056.
[57] Siemens PLM. STARCD v4.34 manual - methodology. 2020.
[58] Shrestha KP, Seidel L, Zeuch T, Mauss F. Detailed kinetic mechanism for the oxidation of ammonia including the formation and reduction of nitrogen oxides. Energy Fuels Oct. 2018;32(10):10202–17. https://doi.org/10.1021/acs.energyfuels.8b01056.
[59] Klippenstein SJ, Harding LB, Glarborg P, Miller JA. The role of NNH in NO formation and control. Combust Flame Apr. 2011;158(4):774–89. https://doi.org/10.1016/j.combustflame.2010.12.013.
[60] Peters N. Turbulent combustion, vol. 12; 2001. https://doi.org/10.1088/0957-0233/12/11/708.
[61] Verhelst S, Tjoen C, Vancoillie J, Demuynck J. A correlation for the laminar burning velocity for use in hydrogen spark ignition engine simulation. Int J Hydrogen Energy Jan. 2011;36(1):957–74. https://doi.org/10.1016/j.ijhydene.2010.10.020.
[62] Altantzis C, Frouzakis CE, Tomboulides AG, Matalon M, Boulouchos K. Hydrodynamic and thermodiffusive instability effects on the evolution of laminar planar lean premixed hydrogen flames. J Fluid Mech Jun. 2012;700:329–61. https://doi.org/10.1017/jfm.2012.136.
[63] Berger L, Attili A, Pitsch H. Synergistic interactions of thermodiffusive instabilities and turbulence in lean hydrogen flames. Combust Flame Oct. 2022;244:112254. https://doi.org/10.1016/j.combustflame.2022.112254.
[64] Hernandez I, Turquand D'Auzay C, Penning R, Shapiro E, Hughes J. Thermo-diffusive flame speed adjustment and its application to hydrogen engines. In: SAE technical papers. SAE International; Apr. 2023. https://doi.org/10.4271/2023-01-0197.
[65] De Bellis V, et al. Development and validation of a phenomenological model for hydrogen fueled PFI internal combustion engines considering Thermo-Diffusive effects on flame speed propagation. Energy Convers Manag May 2024;308:118395. https://doi.org/10.1016/j.enconman.2024.118395.
[66] Ramalho Leite C, Brequigny P, Borée J, Foucher F. Early flame development characterization of ultra-lean hydrogen–air flames in an optical spark-ignition engine. Proc Combust Inst 2024;40(1–4):105260. https://doi.org/10.1016/j.proci.2024.105260.
[67] Sfriso S, et al. Proposal and validation of 3D-CFD framework for ultra-lean hydrogen combustion. ICEs; Apr. 2024. https://doi.org/10.4271/2024-01-2685.
[68] Duan J, Liu F, Sun B. An experimental study on the NOx emission characteristics of PFI hydrogen internal combustion engine. Qiche Gongcheng/Automotive Engineering 2014;36(10).
[69] Kim S, Lee J, Lee S, Lee S, Kim K, Min K. Effects of various compression ratios on a direct injection spark ignition hydrogen-fueled engine in a single-cylinder engine. Int J Automot Technol Jun. 2024. https://doi.org/10.1007/s12239-024-00096-6.
[70] Huang Z, et al. Effects of hydrogen injection timing and injection pressure on mixture formation and combustion characteristics of a hydrogen direct injection engine. Fuel May 2024;363:130966. https://doi.org/10.1016/j.fuel.2024.130966.